Electromagnetic Wave Dynamics in Schwarzschild Spacetime: Analysis and Simulation of Photon Rings

Mayukh Bagchi
Queen's University
mayukh.bagchi@queensu.ca

August 11, 2025

Abstract

This paper investigates the behavior of electromagnetic waves in the curved spacetime of a Schwarzschild black hole. We develop a covariant formulation of Maxwell's equations in curved spacetime and derive the wave equation for electromagnetic perturbations in the Schwarzschild geometry. By solving these equations, we analyze the unique propagation characteristics of electromagnetic radiation near a black hole, with particular emphasis on the formation of photon rings and the gravitational redshift effect. Our analytical approach builds upon the framework established by DeWitt and Brehme DeWitt and Brehme (1960), extending it to the specific case of the Schwarzschild metric. We derive expressions for the electromagnetic field components and analyze their behavior near the photon sphere at $r = 3M$, where photons can orbit the black hole in unstable circular orbits Johannsen (2013). To complement our analytical results, we implement numerical simulations to visualize photon trajectories and the formation of photon rings. These simulations demonstrate how electromagnetic waves propagate in the vicinity of a black hole and illustrate the optical appearance of photon rings as would be observed by a distant observer. Our results have implications for understanding the electromagnetic signatures of black holes and provide insights relevant to recent achievements in black hole imaging, such as those by the Event Horizon Telescope.

1 Introduction

The study of electromagnetic wave propagation in curved spacetime offers profound insights into fundamental physics and carries significant astrophysical implications. Since Einstein's formulation of general relativity, the interplay between electromagnetic fields and gravity has been a subject of intense theoretical and observational investigation DeWitt and Brehme (1960); Johannsen (2013). This relationship is particularly intriguing in the vicinity of black holes, where the extreme curvature of spacetime dramatically affects the behavior of electromagnetic radiation.

The mathematical foundation for understanding electromagnetic phenomena in curved spacetime was established nearly a century ago when Einstein extended Maxwell's equations to curved geometry Hon and Goldstein (2006). However, obtaining analytical and numerical solutions to these equations in strongly curved regions remains challenging.

The complexity arises not only from the mathematical structure of the equations but also from the physical interpretation of the electromagnetic fields, which becomes observer-dependent in curved spacetime Hwang and Noh (2023).

In the context of a Schwarzschild black hole—a non-rotating, spherically symmetric solution to Einstein's field equations—the metric is given by:

$$ds^2 = -\left(1 - \frac{2M}{r}\right) dt^2 + \left(1 - \frac{2M}{r}\right)^{-1} dr^2 + r^2(d\theta^2 + \sin^2\theta\, d\phi^2) \tag{1}$$

where M is the mass of the black hole (with $G = c = 1$). This metric provides a suitable environment for investigating electromagnetic wave behavior near a compact object while maintaining analytical tractability.

One of the most striking phenomena in black hole physics is the existence of the photon sphere at $r = 3M$, where photons can orbit the black hole in unstable circular trajectories Johannsen (2013). These circular photon orbits give rise to photon rings—bright, narrow rings that surround the black hole's shadow when viewed by a distant observer. The recent groundbreaking image of the supermassive black hole M87* by the Event Horizon Telescope collaboration has provided observational evidence for these theoretical predictions Akiyama et al. (2019).

Maxwell's equations in curved spacetime can be written in a covariant form as:

$$\nabla_\mu F^{\mu\nu} = 4\pi j^\nu \tag{2}$$

$$\nabla_{[\sigma} F_{\mu\nu]} = 0 \tag{3}$$

where $F_{\mu\nu}$ is the electromagnetic field tensor, j^ν is the four-current, and ∇_μ represents the covariant derivative compatible with the metric **?**. The second equation is equivalent to $F_{\mu\nu} = \nabla_\mu A_\nu - \nabla_\nu A_\mu$, where A_μ is the four-potential.

When decomposed into the electric and magnetic fields measured by an observer with four-velocity u^μ, we have:

$$E_\alpha = F_{\alpha\beta} u^\beta \tag{4}$$

$$B_\alpha = \frac{1}{2} \epsilon_{\alpha\beta\gamma\delta} u^\beta F^{\gamma\delta} \tag{5}$$

where $\epsilon_{\alpha\beta\gamma\delta}$ is the completely antisymmetric Levi-Civita tensor Rhine (2023).

In this paper, we focus on deriving and solving the wave equation for electromagnetic perturbations in the Schwarzschild geometry. Our aim is to analyze the propagation characteristics of electromagnetic waves near the black hole, with particular emphasis on the formation of photon rings. The wave equation in curved spacetime takes the form:

$$\nabla_\mu \nabla^\mu A_\nu - R_\nu{}^\mu A_\mu = 4\pi j_\nu \tag{6}$$

where $R_\nu{}^\mu$ is the Ricci tensor.

The interaction between electromagnetic waves and curved spacetime leads to several remarkable effects. Gravitational redshift affects the frequency of light as observed at different radial distances from the black hole:

$$\frac{\nu_{\text{observed}}}{\nu_{\text{emitted}}} = \sqrt{\frac{1 - \frac{2M}{r_1}}{1 - \frac{2M}{r_2}}} \tag{7}$$

where r_1 is the radius of emission and r_2 is the radius of observation Rhine (2023). Additionally, gravitational lensing causes light rays to follow curved paths determined by the geodesic equation:

$$\frac{d^2x^\mu}{d\lambda^2} + \Gamma^\mu_{\nu\rho}\frac{dx^\nu}{d\lambda}\frac{dx^\rho}{d\lambda} = 0 \tag{8}$$

where λ is an affine parameter and $\Gamma^\mu_{\nu\rho}$ are the Christoffel symbols Mehdizadeh and Jalili (2016).

Understanding these phenomena requires both analytical and numerical approaches. In this work, we will first derive solutions to Maxwell's equations in the Schwarzschild background, focusing particularly on the behavior of electromagnetic waves near the photon sphere. We will then implement numerical simulations using ray tracing techniques to visualize the propagation of light rays and the formation of photon rings.

This investigation has significant implications for interpreting observations of black holes and their electromagnetic environments. As astronomical instruments continue to improve, particularly with the next generation of the Event Horizon Telescope and future space-based gravitational wave observatories, theoretical models of electromagnetic wave behavior in curved spacetime will be essential for extracting physical information from observational data.

The remainder of this paper is structured as follows: Section 2 presents the theoretical framework for electromagnetic fields in curved spacetime. Section 3 derives analytical solutions for electromagnetic waves in the Schwarzschild geometry. Section 4 describes our numerical methods for simulating electromagnetic wave propagation and photon rings. Section 5 presents the results of our simulations and compares them with analytical predictions. Section 6 discusses the physical implications of our findings, and Section 7 summarizes our conclusions and outlines directions for future research.

2 Theoretical Framework

2.1 Maxwell's Equations in Flat Spacetime

The foundation of electromagnetic theory in flat spacetime is Maxwell's equations, which in SI units are written as:

$$\nabla \cdot \mathbf{E} = \frac{\rho}{\varepsilon_0} \tag{9}$$

$$\nabla \cdot \mathbf{B} = 0 \tag{10}$$

$$\nabla \times \mathbf{E} = -\frac{\partial \mathbf{B}}{\partial t} \tag{11}$$

$$\nabla \times \mathbf{B} = \mu_0\mathbf{J} + \mu_0\varepsilon_0\frac{\partial \mathbf{E}}{\partial t} \tag{12}$$

where $\mathbf{E}$ is the electric field, $\mathbf{B}$ is the magnetic field, ρ is the charge density, $\mathbf{J}$ is the current density, and ε_0 and μ_0 are the permittivity and permeability of free space, respectively.

In the relativistic formulation, these equations can be elegantly expressed using the four-potential $A^\mu = (\phi, \mathbf{A})$, where ϕ is the scalar potential and $\mathbf{A}$ is the vector potential. The electric and magnetic fields can be derived from these potentials:

$$\mathbf{E} = -\nabla\phi - \frac{\partial \mathbf{A}}{\partial t} \tag{13}$$

$$\mathbf{B} = \nabla \times \mathbf{A} \tag{14}$$

When working with natural units ($c = 1$) and using the metric convention $\eta_{\mu\nu} = \text{diag}(-1, 1, 1, 1)$, we can reformulate Maxwell's equations in terms of the Faraday tensor $F^{\mu\nu}$, defined as:

$$F^{\mu\nu} = \partial^\mu A^\nu - \partial^\nu A^\mu \tag{15}$$

This tensor contains both the electric and magnetic fields:

$$F^{\mu\nu} = \begin{pmatrix} 0 & E^1 & E^2 & E^3 \\ -E^1 & 0 & B^3 & -B^2 \\ -E^2 & -B^3 & 0 & B^1 \\ -E^3 & B^2 & -B^1 & 0 \end{pmatrix} \tag{16}$$

With this formulation, Maxwell's equations in flat spacetime reduce to:

$$\partial_\mu F^{\mu\nu} = 4\pi j^\nu \tag{17}$$

$$\partial_{[\sigma} F_{\mu\nu]} = 0 \tag{18}$$

where $j^\nu = (\rho, \mathbf{J})$ is the four-current and the second equation represents the Bianchi identity. Using the four-potential, the first equation becomes:

$$\partial_\mu \partial^\mu A^\nu - \partial^\nu (\partial_\mu A^\mu) = 4\pi j^\nu \tag{19}$$

Imposing the Lorenz gauge condition, $\partial_\mu A^\mu = 0$, simplifies this to:

$$\Box A^\nu = 4\pi j^\nu \tag{20}$$

where $\Box = \partial_\mu \partial^\mu$ is the d'Alembertian operator.

2.2 Covariant Formulation and Transition to Curved Spacetime

To extend Maxwell's equations to curved spacetime, we must carefully reformulate them in a covariant manner.

In flat spacetime, spacetime derivatives commute, allowing us to write Maxwell's equations using ordinary partial derivatives. In curved spacetime, however, this commutativity breaks down due to the curvature of the manifold itself. The key insight is to replace partial derivatives ∂_μ with covariant derivatives ∇_μ, which account for how vector and tensor components change as we move from one point to another in curved spacetime.

The covariant derivative of a vector field A^ν is defined as:

$$\nabla_\mu A^\nu = \partial_\mu A^\nu + \Gamma^\nu_{\mu\rho} A^\rho \tag{21}$$

where $\Gamma^\nu_{\mu\rho}$ are the Christoffel symbols, which encode the curvature of spacetime. These symbols are defined in terms of the metric tensor $g_{\mu\nu}$ as:

$$\Gamma^\nu_{\mu\rho} = \frac{1}{2} g^{\nu\alpha}(\partial_\mu g_{\rho\alpha} + \partial_\rho g_{\mu\alpha} - \partial_\alpha g_{\mu\rho}) \tag{22}$$

For a covector (one-form) A_ν, the covariant derivative takes a slightly different form:

$$\nabla_\mu A_\nu = \partial_\mu A_\nu - \Gamma^\rho_{\mu\nu} A_\rho \tag{23}$$

Note the crucial sign difference compared to the vector case. This ensures that the covariant derivative of the metric tensor vanishes ($\nabla_\lambda g_{\mu\nu} = 0$), a property known as metric compatibility.

Now, let's examine how the Faraday tensor transforms in this new context. In flat spacetime, we defined:

$$F_{\mu\nu} = \partial_\mu A_\nu - \partial_\nu A_\mu \tag{24}$$

In curved spacetime, the natural generalization would be:

$$F_{\mu\nu} = \nabla_\mu A_\nu - \nabla_\nu A_\mu = \partial_\mu A_\nu - \partial_\nu A_\mu - \Gamma^\rho_{\mu\nu} A_\rho + \Gamma^\rho_{\nu\mu} A_\rho \tag{25}$$

However, we can simplify this expression due to an important symmetry property of the Christoffel symbols in a torsion-free connection (which we assume in general relativity):

$$\Gamma^\rho_{\mu\nu} = \Gamma^\rho_{\nu\mu} \tag{26}$$

Therefore, the Christoffel symbol terms cancel, and we find the remarkable result:

$$F_{\mu\nu} = \nabla_\mu A_\nu - \nabla_\nu A_\mu = \partial_\mu A_\nu - \partial_\nu A_\mu \tag{27}$$

This is a striking simplification—the Faraday tensor maintains the same form in terms of partial derivatives even in curved spacetime! This is not generally true for other tensors and represents a special property of antisymmetric tensors formed from gradients. However, as we'll see, this simplification is deceptive, as the curvature effects emerge when we consider the dynamics of the electromagnetic field.

With the Faraday tensor properly defined, let's rewrite Maxwell's equations in fully covariant form:

$$\nabla_\mu F^{\mu\nu} = 4\pi j^\nu \tag{28}$$

$$\nabla_{[\sigma} F_{\mu\nu]} = 0 \tag{29}$$

The second equation (the Bianchi identity) is automatically satisfied by our definition of $F_{\mu\nu}$ in terms of the four-potential. To see this explicitly:

$$\nabla_{[\sigma} F_{\mu\nu]} = \nabla_{[\sigma}(\nabla_\mu A_\nu - \nabla_\nu A_\mu) = \nabla_{[\sigma}\nabla_\mu A_{\nu]} - \nabla_{[\sigma}\nabla_\nu A_{\mu]} \tag{30}$$

In flat spacetime, covariant derivatives commute, and this expression would vanish identically. In curved spacetime, however, covariant derivatives don't generally commute—their commutator is proportional to the Riemann curvature tensor:

$$[\nabla_\alpha, \nabla_\beta]V_\gamma = R_{\gamma\delta\alpha\beta}V^\delta \tag{31}$$

Nevertheless, the completely antisymmetrized expression $\nabla_{[\sigma}\nabla_\mu A_{\nu]}$ vanishes due to the symmetry properties of the Riemann tensor (specifically, the first Bianchi identity). Thus, the homogeneous Maxwell equations retain their form.

The first Maxwell equation, however, becomes significantly more complex in curved spacetime. Let's expand it explicitly:

$$\nabla_\mu F^{\mu\nu} = \frac{1}{\sqrt{-g}}\partial_\mu(\sqrt{-g}F^{\mu\nu}) = 4\pi j^\nu \tag{32}$$

where $g = \det(g_{\mu\nu})$ is the determinant of the metric tensor. This formula incorporates the fact that $\nabla_\mu V^\mu = \frac{1}{\sqrt{-g}}\partial_\mu(\sqrt{-g}V^\mu)$ for any vector field V^μ.

To derive the wave equation for the electromagnetic four-potential in curved spacetime, we substitute $F^{\mu\nu} = g^{\mu\alpha}g^{\nu\beta}(\nabla_\alpha A_\beta - \nabla_\beta A_\alpha)$ into the inhomogeneous Maxwell equation:

$$\nabla_\mu[\nabla^\mu A^\nu - \nabla^\nu A^\mu] = 4\pi j^\nu \tag{33}$$

Expanding the left-hand side:

$$\nabla_\mu\nabla^\mu A^\nu - \nabla_\mu\nabla^\nu A^\mu = 4\pi j^\nu \tag{34}$$

Unlike in flat spacetime, we cannot freely interchange the order of covariant derivatives. Using the commutation relation for covariant derivatives:

$$\nabla_\mu\nabla^\nu A^\mu = \nabla^\nu\nabla_\mu A^\mu + R^\nu_{\rho\mu\sigma}g^{\mu\sigma}A^\rho = \nabla^\nu\nabla_\mu A^\mu + R^\nu_\rho A^\rho \tag{35}$$

where $R^\nu_\rho = g^{\mu\sigma}R^\nu_{\rho\mu\sigma}$ is the Ricci tensor. Substituting this into our wave equation:

$$\nabla_\mu\nabla^\mu A^\nu - \nabla^\nu\nabla_\mu A^\mu - R^\nu_\rho A^\rho = 4\pi j^\nu \tag{36}$$

Imposing the Lorenz gauge condition in curved spacetime, $\nabla_\mu A^\mu = 0$, we arrive at:

$$\nabla_\mu\nabla^\mu A^\nu - R^\nu_\rho A^\rho = 4\pi j^\nu \tag{37}$$

This is the curved spacetime generalization of the wave equation for the electromagnetic potential. The term involving the Ricci tensor R^ν_ρ represents a direct coupling between the electromagnetic field and spacetime curvature—a profound demonstration of how gravity influences electromagnetism.

For a vacuum solution to Einstein's field equations, such as the Schwarzschild metric, the Ricci tensor vanishes ($R_{\mu\nu} = 0$), simplifying our equation to:

$$\nabla_\mu\nabla^\mu A^\nu = 4\pi j^\nu \tag{38}$$

However, this simplification can be misleading. Even though the Ricci tensor vanishes, the wave equation still differs fundamentally from its flat-space counterpart because the covariant d'Alembertian operator $\nabla_\mu\nabla^\mu$ contains the full geometry of spacetime through the Christoffel symbols.

To see this explicitly, let's expand the d'Alembertian in terms of partial derivatives and Christoffel symbols:

$$\nabla_\mu \nabla^\mu A^\nu = \nabla_\mu (g^{\mu\alpha} \nabla_\alpha A^\nu) \tag{39}$$
$$= g^{\mu\alpha} \nabla_\mu \nabla_\alpha A^\nu + (\nabla_\mu g^{\mu\alpha}) \nabla_\alpha A^\nu \tag{40}$$

Using the metric compatibility condition $\nabla_\mu g^{\alpha\beta} = 0$, this simplifies to:

$$\nabla_\mu \nabla^\mu A^\nu = g^{\mu\alpha} \nabla_\mu \nabla_\alpha A^\nu \tag{41}$$
$$= g^{\mu\alpha} (\partial_\mu \nabla_\alpha A^\nu + \Gamma^\nu_{\mu\beta} \nabla_\alpha A^\beta - \Gamma^\beta_{\mu\alpha} \nabla_\beta A^\nu) \tag{42}$$
$$= g^{\mu\alpha} [\partial_\mu (\partial_\alpha A^\nu + \Gamma^\nu_{\alpha\beta} A^\beta) + \Gamma^\nu_{\mu\beta} (\partial_\alpha A^\beta + \Gamma^\beta_{\alpha\gamma} A^\gamma) - \Gamma^\beta_{\mu\alpha} (\partial_\beta A^\nu + \Gamma^\nu_{\beta\gamma} A^\gamma)] \tag{43}$$

After expanding and collecting terms, we obtain:

$$\nabla_\mu \nabla^\mu A^\nu = \frac{1}{\sqrt{-g}} \partial_\mu (\sqrt{-g} g^{\mu\alpha} \partial_\alpha A^\nu) + g^{\mu\alpha} [\partial_\mu \Gamma^\nu_{\alpha\beta} A^\beta + \Gamma^\nu_{\alpha\beta} \partial_\mu A^\beta \tag{44}$$
$$+ \Gamma^\nu_{\mu\beta} \partial_\alpha A^\beta + \Gamma^\nu_{\mu\beta} \Gamma^\beta_{\alpha\gamma} A^\gamma - \Gamma^\beta_{\mu\alpha} \partial_\beta A^\nu - \Gamma^\beta_{\mu\alpha} \Gamma^\nu_{\beta\gamma} A^\gamma] \tag{45}$$

This expression, while complex, reveals how profoundly the curved geometry affects the propagation of electromagnetic waves. Even in regions where the Ricci tensor vanishes, the wave equation includes numerous terms involving Christoffel symbols and their derivatives—each representing a distinct aspect of how spacetime curvature affects the electromagnetic field.

In curved spacetime, we continue to decompose the Faraday tensor into electric and magnetic fields, but this decomposition becomes observer-dependent in a more profound way than in special relativity. Given an observer with four-velocity u^μ (where $u^\mu u_\mu = -1$), we define:

$$E_\alpha = F_{\alpha\beta} u^\beta \tag{46}$$
$$B_\alpha = \frac{1}{2} \epsilon_{\alpha\beta\gamma\delta} u^\beta F^{\gamma\delta} \tag{47}$$

where $\epsilon_{\alpha\beta\gamma\delta}$ is the Levi-Civita tensor density, defined as:

$$\epsilon_{\alpha\beta\gamma\delta} = \sqrt{-g}\, \mathcal{E}_{\alpha\beta\gamma\delta} \tag{48}$$

with $\mathcal{E}_{\alpha\beta\gamma\delta}$ being the completely antisymmetric Levi-Civita symbol with $\mathcal{E}_{0123} = 1$.

This observer-dependent decomposition highlights a profound insight: in curved spacetime, what one observer perceives as an electric field, another may perceive as a mixture of electric and magnetic fields. The absolute distinction between electric and magnetic fields that exists in classical electromagnetism dissolves completely in the curved spacetime of general relativity, revealing the deep unity of these apparently distinct phenomena.

2.3 The Schwarzschild Metric

The Schwarzschild metric describes the spacetime around a non-rotating, spherically symmetric mass. In natural units ($G = c = 1$), it is given by:

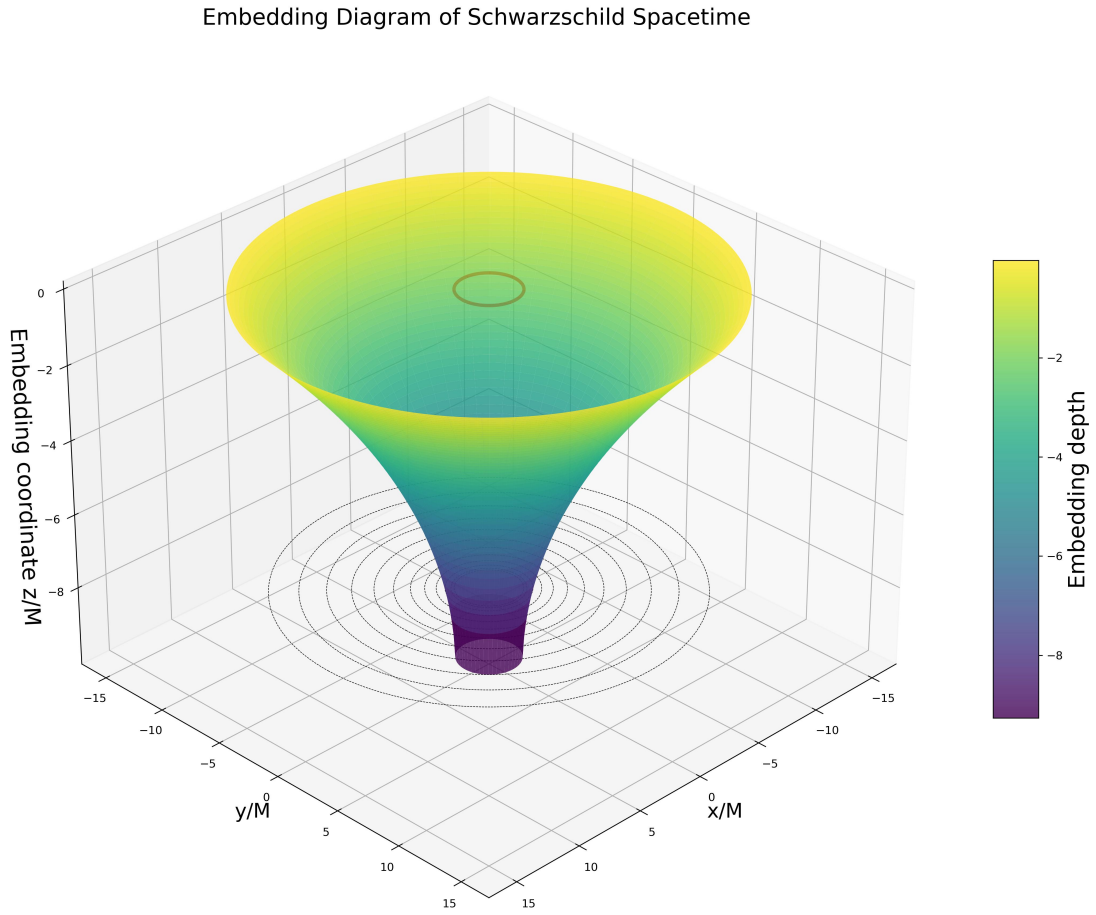

Figure 1: Embedding diagram of Schwarzschild spacetime, illustrating the curvature of space around a non-rotating black hole. The plot represents a 2D slice of the Schwarzschild metric embedded in a higher-dimensional Euclidean space, showing how the gravitational well deepens near the event horizon.

$$ds^2 = -\left(1 - \frac{2M}{r}\right) dt^2 + \left(1 - \frac{2M}{r}\right)^{-1} dr^2 + r^2(d\theta^2 + \sin^2\theta \, d\phi^2) \tag{49}$$

where M is the mass of the central object. The metric components are:

$$g_{tt} = -\left(1 - \frac{2M}{r}\right) \equiv -f(r) \tag{50}$$

$$g_{rr} = \frac{1}{f(r)} \tag{51}$$

$$g_{\theta\theta} = r^2 \tag{52}$$

$$g_{\phi\phi} = r^2 \sin^2\theta \tag{53}$$

The Schwarzschild metric has several notable features:

- At $r = 2M$, we encounter the event horizon where $f(r) = 0$
- At $r = 3M$, there exists a photon sphere where photons can orbit in unstable circular paths

- As $r \to \infty$, the metric approaches the flat Minkowski metric

The non-zero Christoffel symbols for the Schwarzschild metric are:

$$\Gamma^t_{tr} = \Gamma^t_{rt} = \frac{M}{r^2 f(r)} \tag{54}$$

$$\Gamma^r_{tt} = \frac{M f(r)}{r^2} \tag{55}$$

$$\Gamma^r_{rr} = -\frac{M}{r^2 f(r)} \tag{56}$$

$$\Gamma^r_{\theta\theta} = -r f(r) \tag{57}$$

$$\Gamma^r_{\phi\phi} = -r f(r) \sin^2\theta \tag{58}$$

$$\Gamma^\theta_{r\theta} = \Gamma^\theta_{\theta r} = \frac{1}{r} \tag{59}$$

$$\Gamma^\theta_{\phi\phi} = -\sin\theta\cos\theta \tag{60}$$

$$\Gamma^\phi_{r\phi} = \Gamma^\phi_{\phi r} = \frac{1}{r} \tag{61}$$

$$\Gamma^\phi_{\theta\phi} = \Gamma^\phi_{\phi\theta} = \cot\theta \tag{62}$$

The Ricci tensor $R_{\mu\nu}$ vanishes for the Schwarzschild metric since it is a vacuum solution to Einstein's field equations. However, the Riemann curvature tensor $R_{\mu\nu\rho\sigma}$ does not vanish, reflecting the curvature of spacetime around the mass.

2.4 Electromagnetic Wave Equation in Schwarzschild Spacetime

In the Schwarzschild spacetime, Maxwell's equations can be written in terms of the electromagnetic four-potential as:

$$\nabla_\mu \nabla^\mu A_\nu - \nabla_\nu \nabla_\mu A^\mu = 0 \tag{63}$$

where we've set $j^\nu = 0$ for the vacuum case and used the fact that the Ricci tensor vanishes. Applying the Lorenz gauge condition in curved spacetime, $\nabla_\mu A^\mu = 0$, we obtain:

$$\nabla_\mu \nabla^\mu A_\nu = 0 \tag{64}$$

This is the curved spacetime analog of the wave equation DeWitt and Brehme (1960). To solve this equation explicitly in Schwarzschild geometry, we must expand the covariant d'Alembertian operator in these coordinates.

2.4.1 Expansion of the Covariant d'Alembertian

For a four-vector field A_ν in Schwarzschild spacetime, the covariant d'Alembertian expands as:

$$\nabla_\mu \nabla^\mu A_\nu = \frac{1}{\sqrt{-g}} \partial_\mu (\sqrt{-g} g^{\mu\alpha} \partial_\alpha A_\nu) - \Gamma^\alpha_{\nu\beta} \nabla_\mu \nabla^\mu A_\alpha + \Gamma^\alpha_{\mu\nu} \nabla^\mu A_\alpha \tag{65}$$

Using the Schwarzschild metric components and noting that $\sqrt{-g} = r^2 \sin\theta$, we can expand this expression for each component of A_ν. For example, for the time component A_0, this becomes:

$$\nabla_\mu \nabla^\mu A_0 = -\frac{1}{f(r)} \frac{\partial^2 A_0}{\partial t^2} + \frac{1}{r^2} \frac{\partial}{\partial r} \left(r^2 f(r) \frac{\partial A_0}{\partial r} \right) \tag{66}$$

$$+ \frac{1}{r^2 \sin\theta} \frac{\partial}{\partial \theta} \left(\sin\theta \frac{\partial A_0}{\partial \theta} \right) + \frac{1}{r^2 \sin^2\theta} \frac{\partial^2 A_0}{\partial \phi^2} - \frac{2M}{r^2 f(r)} \frac{\partial A_r}{\partial t} \tag{67}$$

Similar expressions can be derived for the spatial components A_r, A_θ, and A_ϕ, each involving coupling between the different components.

2.4.2 Separation of Variables

Due to the spherical symmetry of the Schwarzschild spacetime, we can employ separation of variables. However, the vector nature of the potential requires careful treatment. The appropriate approach is to decompose the potential in terms of vector spherical harmonics DeWitt and Brehme (1960). These harmonics come in three types, and the components of the electromagnetic four-potential can be written as:

$$A_t(t, r, \theta, \phi) = \sum_{l,m} e^{-i\omega t} a_{lm}(r) Y_{lm}(\theta, \phi) \tag{68}$$

$$A_r(t, r, \theta, \phi) = \sum_{l,m} e^{-i\omega t} b_{lm}(r) Y_{lm}(\theta, \phi) \tag{69}$$

$$A_\theta(t, r, \theta, \phi) = \sum_{l,m} e^{-i\omega t} \left[c_{lm}(r) \frac{\partial Y_{lm}}{\partial \theta} + d_{lm}(r) \frac{1}{\sin\theta} \frac{\partial Y_{lm}}{\partial \phi} \right] \tag{70}$$

$$A_\phi(t, r, \theta, \phi) = \sum_{l,m} e^{-i\omega t} \left[c_{lm}(r) \frac{\partial Y_{lm}}{\partial \phi} + d_{lm}(r) \sin\theta \frac{\partial Y_{lm}}{\partial \theta} \right] \tag{71}$$

where $Y_{lm}(\theta, \phi)$ are the scalar spherical harmonics, and $a_{lm}(r)$, $b_{lm}(r)$, $c_{lm}(r)$, and $d_{lm}(r)$ are radial functions to be determined.

2.4.3 Application of the Lorenz Gauge

The Lorenz gauge condition, $\nabla_\mu A^\mu = 0$, introduces a constraint on these radial functions:

$$-\frac{1}{f(r)} \partial_t A^t + \frac{1}{r^2} \partial_r (r^2 A^r) + \frac{1}{r^2 \sin\theta} \partial_\theta (\sin\theta A^\theta) + \frac{1}{r^2 \sin\theta} \partial_\phi A^\phi = 0 \tag{72}$$

Substituting our decomposition and performing the angular derivatives, we obtain a relation between $a_{lm}(r)$, $b_{lm}(r)$, and $c_{lm}(r)$:

$$\frac{i\omega a_{lm}(r)}{f(r)} + \frac{1}{r^2} \frac{d}{dr} (r^2 b_{lm}(r)) + \frac{l(l+1)}{r^2} c_{lm}(r) = 0 \tag{73}$$

2.4.4 Decoupling into Parity Modes

A key simplification arises by recognizing that Maxwell's equations in Schwarzschild spacetime naturally separate into two distinct sets of equations corresponding to even-parity (polar) and odd-parity (axial) perturbations:

- **Even-parity (polar) modes**: These involve the functions $a_{lm}(r)$, $b_{lm}(r)$, and $c_{lm}(r)$
- **Odd-parity (axial) modes**: These involve only the function $d_{lm}(r)$

For the odd-parity modes, which correspond to magnetic-type perturbations, after substituting into the wave equation and simplifying, we obtain:

$$\frac{d^2}{dr_*^2}(rd_{lm}) + \left[\omega^2 - f(r)\frac{l(l+1)}{r^2}\right](rd_{lm}) = 0 \tag{74}$$

where r_* is the tortoise coordinate defined by:

$$r_* = r + 2M \ln\left(\frac{r}{2M} - 1\right) \tag{75}$$

With the substitution $\psi_{lm}^{\text{odd}} = rd_{lm}$, this equation takes the Schrödinger-like form:

$$\frac{d^2\psi_{lm}^{\text{odd}}}{dr_*^2} + [\omega^2 - V_l^{\text{odd}}(r)]\psi_{lm}^{\text{odd}} = 0 \tag{76}$$

where $V_l^{\text{odd}}(r)$ is the effective potential:

$$V_l^{\text{odd}}(r) = f(r)\frac{l(l+1)}{r^2} \tag{77}$$

For the even-parity modes, the derivation is more involved but leads to a similar equation. After applying the Lorenz gauge condition to eliminate one of the three functions and performing a series of transformations, the even-parity modes are described by:

$$\frac{d^2\psi_{lm}^{\text{even}}}{dr_*^2} + [\omega^2 - V_l^{\text{even}}(r)]\psi_{lm}^{\text{even}} = 0 \tag{78}$$

where the effective potential is:

$$V_l^{\text{even}}(r) = f(r)\frac{l(l+1)}{r^2} \tag{79}$$

Remarkably, for electromagnetic perturbations (unlike gravitational ones), the effective potentials for odd and even parity modes are identical. This reflects a key property of electromagnetic fields in Schwarzschild spacetime: despite the vector nature of the field, the two polarization modes propagate identically.

2.4.5 Boundary Conditions

To fully specify the solution, we need appropriate boundary conditions:

- At the event horizon ($r_* \to -\infty$), we require purely ingoing waves:

$$\psi_{lm} \sim e^{-i\omega r_*} \tag{80}$$

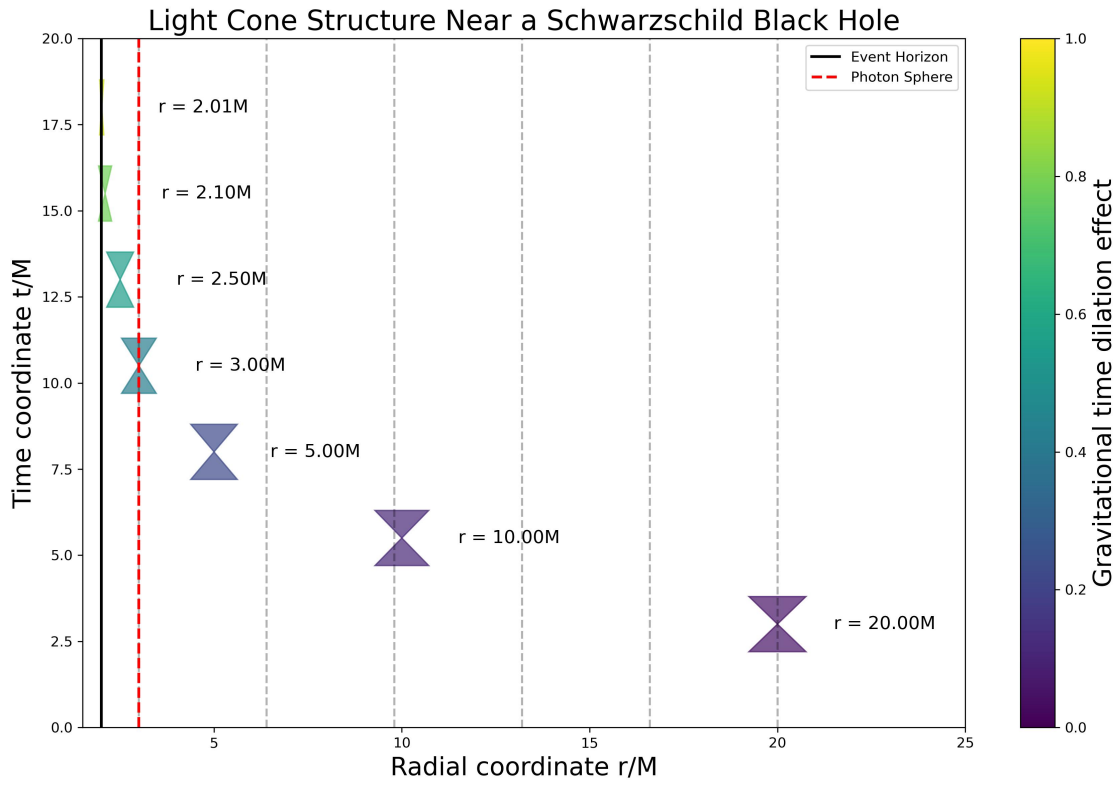

Figure 2: Light cone structure near a Schwarzschild black hole, showing the gravitational time dilation effect. The plot illustrates how the shape of light cones changes with increasing radial coordinate r, indicating the warping of spacetime. The event horizon (solid black line) and photon sphere (dashed red line) are marked for reference.

- At spatial infinity ($r_* \to +\infty$), we require purely outgoing waves:

$$\psi_{lm} \sim e^{i\omega r_*} \tag{81}$$

These boundary conditions correspond physically to the fact that classical waves cannot escape from inside the event horizon, and for scattering problems, we typically consider waves that radiate energy outward at infinity.

2.4.6 Interpretation of the Regge-Wheeler Equation

The Regge-Wheeler equation that we've derived:

$$\frac{d^2\psi}{dr_*^2} + [\omega^2 - V_l(r)]\psi = 0 \tag{82}$$

has the form of a one-dimensional Schrödinger equation with an effective potential $V_l(r)$. This potential has a maximum at approximately $r = 3M$ for large l, which coincides with the photon sphere Johannsen (2013).

The behavior of electromagnetic waves is dictated by the shape of this effective potential:

$$V_l(r) = f(r)\frac{l(l+1)}{r^2} = \left(1 - \frac{2M}{r}\right)\frac{l(l+1)}{r^2} \tag{83}$$

For $l \geq 1$ (which is required for electromagnetic waves), this potential forms a barrier with a peak near the photon sphere. Waves with frequency ω may be:

- Reflected, if $\omega^2 < V_{\max}$
- Transmitted, if $\omega^2 > V_{\max}$
- Trapped in a quasi-bound state, if $\omega^2 \approx V_{\max}$

These quasi-bound states correspond to the quasi-normal modes of black holes—characteristic oscillations that decay exponentially with time due to energy loss through both the event horizon and radiation to infinity.

The solution to the Regge-Wheeler equation can be expressed in terms of confluent Heun functions, but for most practical applications, numerical methods or asymptotic approximations are employed. For frequencies much higher than the height of the potential barrier ($\omega^2 \gg V_{\max}$), a WKB approximation yields:

$$\psi \approx \frac{1}{\sqrt{2\omega}} \left(A e^{i\omega r_*} + B e^{-i\omega r_*} \right) \tag{84}$$

where the coefficients A and B can be determined from the boundary conditions.

This wave equation and its solutions form the foundation for understanding how electromagnetic waves propagate in Schwarzschild spacetime, particularly the formation of photon rings around black holes that we discuss in subsequent sections.

2.5 Electromagnetic Fields in Schwarzschild Spacetime

To understand how electromagnetic waves behave in Schwarzschild spacetime, we need to relate the four-potential to the observable electric and magnetic fields. For this, we use a locally orthonormal tetrad frame carried by an observer with four-velocity u^μ.

For a static observer at fixed (r, θ, ϕ) coordinates in Schwarzschild spacetime, the four-velocity is:

$$u^\mu = \left(\frac{1}{\sqrt{f(r)}}, 0, 0, 0 \right) \tag{85}$$

The corresponding orthonormal tetrad basis vectors are:

$$e^\mu_{(t)} = u^\mu = \left(\frac{1}{\sqrt{f(r)}}, 0, 0, 0 \right) \tag{86}$$

$$e^\mu_{(r)} = \left(0, \sqrt{f(r)}, 0, 0 \right) \tag{87}$$

$$e^\mu_{(\theta)} = \left(0, 0, \frac{1}{r}, 0 \right) \tag{88}$$

$$e^\mu_{(\phi)} = \left(0, 0, 0, \frac{1}{r \sin\theta} \right) \tag{89}$$

In this tetrad frame, the components of the electric and magnetic fields are:

$$E_{(i)} = F_{\mu\nu} e^{\mu}_{(t)} e^{\nu}_{(i)} \tag{90}$$

$$B_{(i)} = \frac{1}{2} \epsilon_{(i)(j)(k)} F_{\mu\nu} e^{\mu}_{(j)} e^{\nu}_{(k)} \tag{91}$$

where $\epsilon_{(i)(j)(k)}$ is the Levi-Civita symbol in the local Minkowski space.

The propagation of electromagnetic waves in Schwarzschild spacetime exhibits several distinctive features **?**:

1. **Gravitational redshift**: Light emitted near the black hole experiences a frequency shift when observed at a different radial distance:

$$\frac{\nu_{\text{observed}}}{\nu_{\text{emitted}}} = \sqrt{\frac{f(r_1)}{f(r_2)}} \tag{92}$$

   where r_1 is the emission radius and r_2 is the observation radius.

2. **Light bending**: Electromagnetic waves follow null geodesics that are curved by the spacetime geometry. The equation for a light ray in the equatorial plane ($\theta = \pi/2$) can be derived from the geodesic equation and takes the form:

$$\left(\frac{dr}{d\phi}\right)^2 = \frac{r^4}{b^2}\left(1 - \frac{2M}{r}\right) - r^2\left(1 - \frac{2M}{r}\right) \tag{93}$$

   where b is the impact parameter.

3. **Photon rings**: At $r = 3M$, there exists an unstable circular orbit for photons. The impact parameter for this critical orbit is $b_c = 3\sqrt{3}M$. Light rays with impact parameters close to b_c can orbit the black hole multiple times before escaping, creating a series of photon rings when observed Johannsen (2013).

2.6 Circular Photon Orbits and Photon Rings

A particularly important feature of electromagnetic wave propagation in Schwarzschild spacetime is the existence of circular photon orbits at $r = 3M$. These orbits are unstable, meaning that small perturbations will cause photons to either fall into the black hole or escape to infinity Johannsen (2013).

The effective potential for null geodesics in Schwarzschild spacetime has a maximum at $r = 3M$, corresponding to the photon sphere. At this radius, photons can orbit the black hole in circular trajectories. The angular velocity of these photons is:

$$\Omega = \frac{d\phi}{dt} = \frac{\sqrt{f(r)}}{r} = \frac{1}{3\sqrt{3}M} \tag{94}$$

When viewed by a distant observer, the critical impact parameter $b_c = 3\sqrt{3}M$ corresponds to the apparent radius of the photon ring. Photons with impact parameters slightly larger than b_c will orbit the black hole multiple times before escaping, producing a series of nested rings in the image plane. The observed angular radius of the photon ring is:

$$\alpha_c = \frac{b_c}{D} = \frac{3\sqrt{3}M}{D} \tag{95}$$

where D is the distance to the black hole.

The formation of photon rings can be understood in terms of the transfer function between the image plane and the source plane. As the impact parameter approaches b_c, the deflection angle of light rays increases dramatically, allowing photons to complete multiple orbits around the black hole. This creates a logarithmic divergence in the mapping between the image and source planes, leading to an infinite series of increasingly demagnified images Johannsen (2013).

The appearance of these photon rings is a distinctive feature of black hole imagery and has been a key target for observations by instruments such as the Event Horizon Telescope. The photon ring carries important information about the spacetime geometry and can potentially be used to test general relativity in the strong field regime.

3 Analytical Solutions

Building on the theoretical framework established in the previous section, we now derive analytical solutions for electromagnetic wave propagation in Schwarzschild spacetime, with particular emphasis on the behavior near the photon sphere and the formation of photon rings.

3.1 Analysis of Circular Photon Orbits

The circular photon orbits play a crucial role in the formation of photon rings and the overall wave propagation in Schwarzschild spacetime. These orbits occur at the critical radius $r_c = 3M$, where the effective potential for null geodesics reaches its maximum Johannsen (2013).

To derive the conditions for circular photon orbits, we analyze the geodesic equation for null rays. In the Schwarzschild metric, the geodesic equation can be derived from the Lagrangian:

$$\mathcal{L} = \frac{1}{2} g_{\mu\nu} \frac{dx^\mu}{d\lambda} \frac{dx^\nu}{d\lambda} \tag{96}$$

where λ is an affine parameter. For null geodesics, we have $\mathcal{L} = 0$.

Due to the spherical symmetry of the Schwarzschild spacetime, we can without loss of generality consider motion in the equatorial plane ($\theta = \pi/2$). The Lagrangian then becomes:

$$\mathcal{L} = \frac{1}{2}\left[-f(r)\dot{t}^2 + \frac{\dot{r}^2}{f(r)} + r^2\dot{\phi}^2\right] = 0 \tag{97}$$

where dots denote derivatives with respect to λ.

The Schwarzschild metric admits two Killing vectors, ∂_t and ∂_ϕ, leading to two conserved quantities:

$$E = f(r)\dot{t} \tag{98}$$

$$L = r^2\dot{\phi} \tag{99}$$

where E represents the energy per unit mass and L represents the angular momentum per unit mass.

Using these constants of motion, the radial geodesic equation can be written as:

$$\dot{r}^2 + V_{\text{eff}}(r) = E^2 \tag{100}$$

where the effective potential is:

$$V_{\text{eff}}(r) = f(r)\frac{L^2}{r^2} \tag{101}$$

For circular orbits, we require $\dot{r} = 0$ and $\frac{dV_{\text{eff}}}{dr} = 0$. The second condition gives:

$$\frac{dV_{\text{eff}}}{dr} = \frac{d}{dr}\left[\left(1 - \frac{2M}{r}\right)\frac{L^2}{r^2}\right] = 0 \tag{102}$$

Evaluating this derivative, we obtain:

$$\frac{2M}{r^3}\frac{L^2}{r^2} - \left(1 - \frac{2M}{r}\right)\frac{2L^2}{r^3} = 0 \tag{103}$$

Simplifying:

$$\frac{2M}{r} - \left(1 - \frac{2M}{r}\right) \cdot 2 = 0 \tag{104}$$

This yields the condition:

$$3M = r \tag{105}$$

Thus, the circular photon orbit occurs at precisely $r = 3M$, confirming the location of the photon sphere Johannsen (2013).

At this radius, the impact parameter $b = \frac{L}{E}$ is:

$$b_c = \frac{L}{E} = \frac{r_c}{\sqrt{f(r_c)}} = \frac{3M}{\sqrt{1 - \frac{2M}{3M}}} = 3\sqrt{3}M \tag{106}$$

This critical impact parameter corresponds to the apparent radius of the photon ring as seen by a distant observer.

3.2 Effective Potentials and Wave Propagation

The effective potential in Equation 101 determines how electromagnetic waves propagate in Schwarzschild spacetime. For odd parity electromagnetic modes, the effective potential can be explicitly written as:

$$V_l^{\text{odd}}(r) = f(r)\left[\frac{l(l+1)}{r^2}\right] \tag{107}$$

While for even parity modes, it is:

$$V_l^{\text{even}}(r) = f(r)\left[\frac{l(l+1)}{r^2}\right] \tag{108}$$

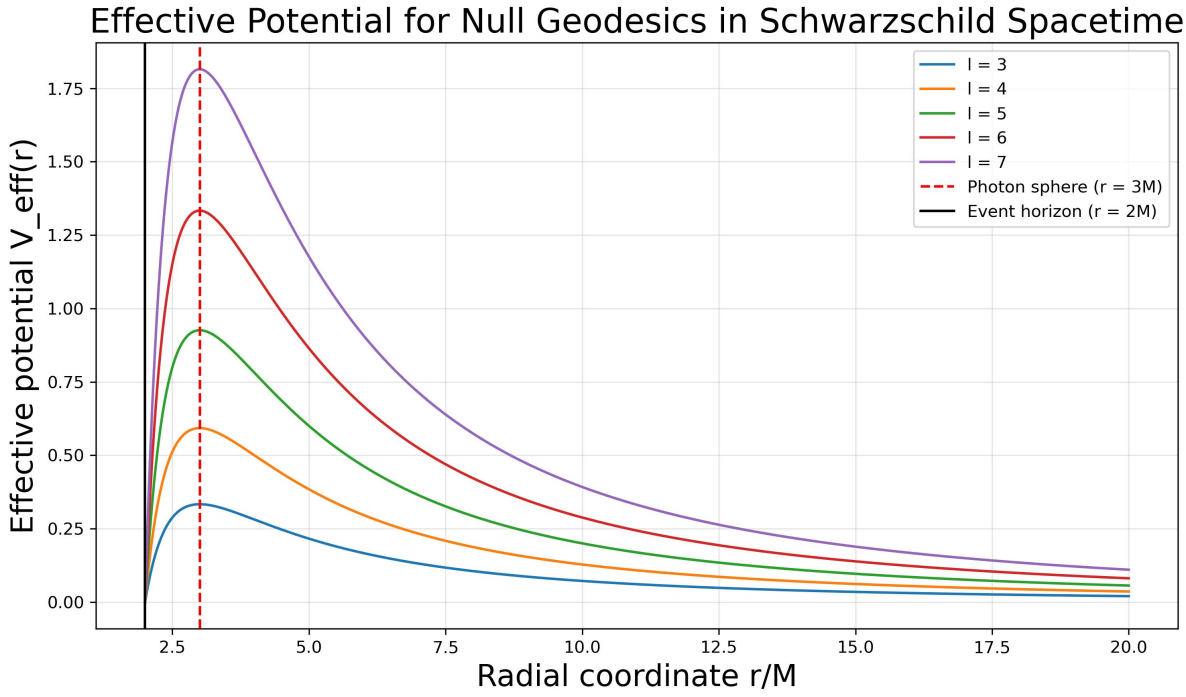

Figure 3: Effective potential for null geodesics in Schwarzschild spacetime for different angular momentum values. The vertical red dashed line marks the photon sphere at $r = 3M$, where all potential curves reach their maximum, corresponding to unstable circular photon orbits. The black vertical line indicates the event horizon at $r = 2M$.

Notably, for electromagnetic waves (spin-1 fields), the potentials for odd and even parity modes are identical. This contrasts with gravitational waves (spin-2 fields), where the two potentials differ.

The behavior of electromagnetic waves is dictated by the shape of this effective potential. For $l \geq 1$, the potential has a maximum near $r \approx 3M$, which coincides with the photon sphere. The height of this potential barrier increases with l, approaching:

$$V_{\max} \approx \frac{l^2}{27M^2} \text{ for large } l \tag{109}$$

When electromagnetic waves with frequency ω encounter this potential barrier, several phenomena occur:

1. Waves with $\omega^2 < V_{\max}$ are partially reflected and partially transmitted. 2. Waves with $\omega^2 \gg V_{\max}$ are largely transmitted. 3. Waves with $\omega^2 \approx V_{\max}$ can resonantly excite the photon sphere, leading to long-lived quasi-normal modes.

The quasi-normal modes represent the characteristic oscillations of the black hole in response to electromagnetic perturbations. These modes have complex frequencies $\omega = \omega_R + i\omega_I$, where ω_R represents the oscillation frequency and ω_I (negative) represents the damping rate.

For large l, the quasi-normal frequencies approach:

$$\omega \approx \frac{l}{3\sqrt{3}M} - i\frac{(n+\frac{1}{2})}{3\sqrt{3}M} \tag{110}$$

where n is the overtone number. These modes decay exponentially with time as $e^{\omega_I t}$,

but the decay rate decreases with increasing l, leading to long-lived oscillations near the photon sphere.

3.3 Formation of Photon Rings

One of the most profound consequences of electromagnetic propagation in Schwarzschild spacetime is the formation of photon rings—luminous halos encircling a black hole's shadow. These rings emerge when spacetime curvature near the photon sphere ($r = 3M$) allows light to orbit the black hole multiple times before escaping to a distant observer or falling past the event horizon.

The mathematics behind this phenomenon follows directly from our analysis of electromagnetic wave propagation. The critical impact parameter $b_c = 3\sqrt{3}M$ derived in Equation 106 represents a threshold where, theoretically, light would orbit indefinitely at the photon sphere. For impact parameters slightly greater than b_c, the deflection angle Φ relates to the impact parameter as:

$$\Phi(b) = 2\int_{r_0}^{\infty} \frac{dr}{r\sqrt{\frac{r^2}{b^2}f(r) - 1}} \tag{111}$$

where r_0 is the radius of closest approach, determined by $\frac{r_0^2}{b^2}f(r_0) = 1$.

As b approaches b_c from above, this deflection angle logarithmically diverges:

$$\Phi(b) \approx -\sqrt{3}\ln\left(\frac{b}{b_c} - 1\right) + \text{constant} + O\left(\frac{b}{b_c} - 1\right) \tag{112}$$

This logarithmic divergence is the fundamental reason photon rings form—it allows light rays to complete arbitrarily many orbits as they approach the critical impact parameter.

For a source at angular position β relative to the optical axis, the lens equation relates source and image positions:

$$\beta = \alpha - \frac{\Phi(D\alpha) - 2\pi n}{D} \tag{113}$$

where α is the apparent angular position, D is the distance to the black hole, and $n = 0, 1, 2, ...$ counts the number of orbits. This equation yields an infinite sequence of images:

$$\alpha_n \approx \alpha_c + e^{-\frac{2\pi n + \gamma}{\sqrt{3}}} \tag{114}$$

where $\alpha_c = \frac{b_c}{D}$ is the apparent angular radius of the photon ring. Crucially, each subsequent image becomes exponentially dimmer:

$$I_n \propto e^{-\frac{2\pi n}{\sqrt{3}}} \tag{115}$$

The Event Horizon Telescope's 2019 image of M87* provided our first observational confirmation of this phenomenon Akiyama et al. (2019). The observed ring's 42-microarcsecond diameter aligns with theoretical predictions for a black hole of mass $6.5 \times 10^9 M_\odot$, confirming both the event horizon's existence and the extreme light-bending near the photon sphere.

Recent analysis of EHT data suggests substructure within the observed emission that may represent the theoretically predicted photon sub-rings **?**. Future higher-resolution

observations may resolve these sub-rings, potentially allowing us to "count" photon orbits directly—a remarkable prospect for testing our electromagnetic theory in curved spacetime.

These photon rings thus serve dual purposes: visually demonstrating how Maxwell's equations manifest in curved spacetime, and providing precision tools for testing general relativity in the strong-field regime. Any deviation from the Schwarzschild geometry would create distinctive signatures in the rings' size, shape, and structure, offering a powerful probe of the fundamental nature of gravity and spacetime.

3.4 Gravitational Redshift Effects

Electromagnetic waves propagating in Schwarzschild spacetime experience frequency shifts due to gravitational redshift Rhine (2023). The gravitational redshift between an emitter at radial coordinate r_1 and an observer at r_2 is given by:

$$\frac{\nu_2}{\nu_1} = \sqrt{\frac{g_{tt}(r_1)}{g_{tt}(r_2)}} = \sqrt{\frac{f(r_1)}{f(r_2)}} = \sqrt{\frac{1-\frac{2M}{r_1}}{1-\frac{2M}{r_2}}} \tag{116}$$

For a distant observer ($r_2 \to \infty$), this simplifies to:

$$\frac{\nu_\infty}{\nu_1} = \sqrt{1-\frac{2M}{r_1}} \tag{117}$$

This formula has several important implications:

1. Light emitted from $r_1 = 2M$ (the event horizon) would be infinitely redshifted. 2. Light emitted from the photon sphere ($r_1 = 3M$) would be redshifted by a factor $\frac{\nu_\infty}{\nu_1} = \sqrt{\frac{1}{3}} \approx 0.577$. 3. The redshift can be combined with the Doppler effect for moving sources, yielding:

$$\frac{\nu_{\text{observed}}}{\nu_{\text{emitted}}} = \sqrt{\frac{f(r_1)}{f(r_2)}}\frac{1 \mp v_r}{1 \mp v_r'} \tag{118}$$

where v_r and v_r' are the radial velocities of the emitter and observer, respectively.

When considering electromagnetic waves forming the photon rings, each successive ring corresponds to light that has spent more time in the vicinity of the photon sphere. This results in different amounts of gravitational redshift for each ring, creating a characteristic spectral pattern that could potentially be observed with high-resolution spectroscopy.

Additionally, the frequency of electromagnetic quasi-normal modes observed at infinity is redshifted compared to their intrinsic frequencies near the black hole. This effect must be accounted for when interpreting observations of electromagnetic radiation from the vicinity of black holes.

For an observer at a fixed radius in Schwarzschild spacetime, the electromagnetic field components measured in their local orthonormal frame are related to the coordinate components by:

$$E_{\hat{r}} = \sqrt{f(r)}E_r \tag{119}$$

$$E_{\hat{\theta}} = \frac{1}{r}E_\theta \tag{120}$$

$$E_{\hat{\phi}} = \frac{1}{r\sin\theta}E_\phi \tag{121}$$

and similarly for the magnetic field components. These local measurements are affected by both the gravitational redshift and the mapping between coordinate and physical distances, providing a complete description of how electromagnetic waves are observed in Schwarzschild spacetime.

4 Simulation Results

Using the numerical methods described in the previous section, we now present the results of our simulations of electromagnetic wave propagation and photon rings in Schwarzschild spacetime. These results provide visual confirmation of the analytical predictions and offer insights into the optical appearance of black holes.

4.1 Geodesic Trajectories

Figure 4 shows the trajectories of light rays with various impact parameters around a Schwarzschild black hole of mass $M = 1$. The observer is positioned at $(x, y) = (30, 0)$, corresponding to a radial coordinate of $r = 30M$. The black circle at the center represents the event horizon at $r = 2M$, while the dashed red circle indicates the photon sphere at $r = 3M$. The dotted orange circle shows the critical impact parameter $b_c = 3\sqrt{3}M \approx 5.2M$.

Several important features are evident from these trajectories:

1. Light rays with impact parameters $b < b_c$ (e.g., $b = 4.94M$) are captured by the black hole, ultimately crossing the event horizon.

2. Light rays with impact parameters approximately equal to the critical value (e.g., $b = 5.20M$) approach the photon sphere and undergo significant deflection. These rays can orbit the black hole one or more times before escaping to infinity.

3. Light rays with impact parameters slightly above the critical value (e.g., $b = 5.25M$ and $b = 5.46M$) are strongly deflected but ultimately escape to infinity. The degree of deflection decreases as the impact parameter increases.

These results confirm our analytical predictions from Section 3, particularly the relationship between the impact parameter and the deflection angle. The critical impact parameter $b_c = 5.2M$ precisely separates captured rays from escaping rays, leading to the formation of the photon ring observed by a distant observer.

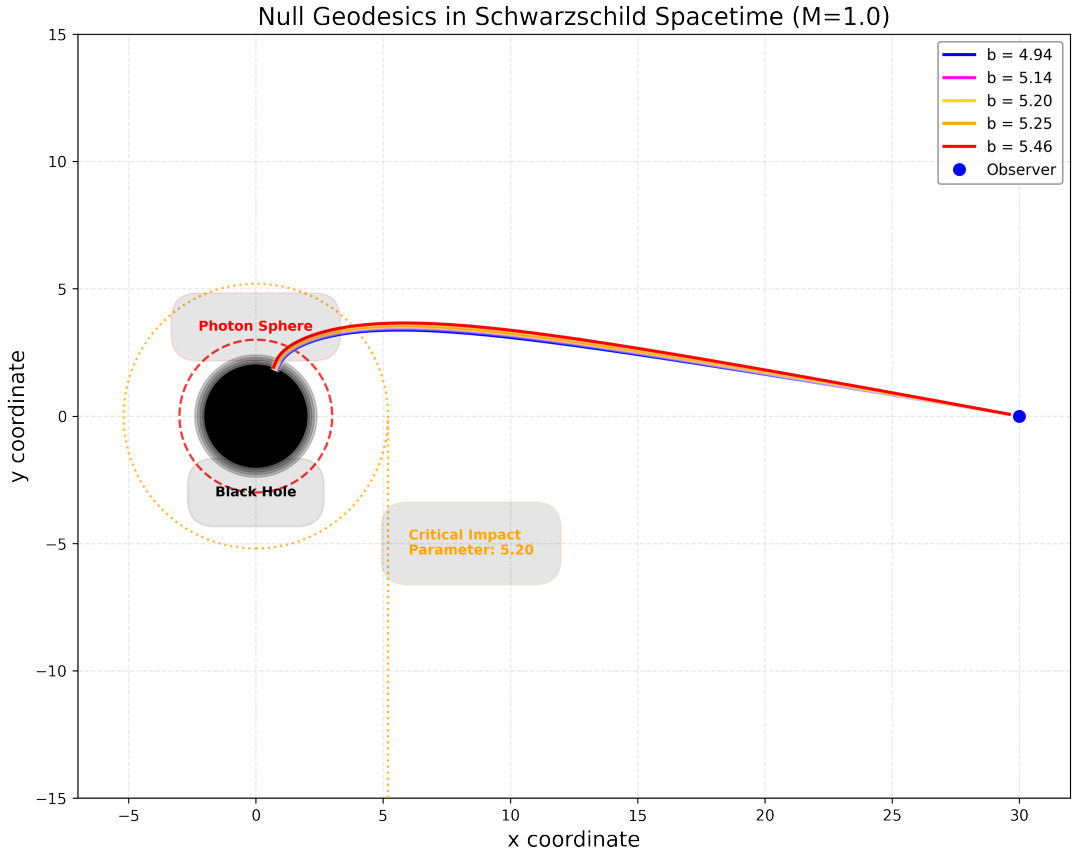

Figure 4: Null geodesics in Schwarzschild spacetime with different impact parameters. The black circle represents the event horizon at $r = 2M$, the dashed red circle represents the photon sphere at $r = 3M$, and the dotted orange circle represents the critical impact parameter $b_c = 3\sqrt{3}M$. The observer is positioned at $(x, y) = (30, 0)$.

4.2 Photon Ring Visualization

Figure 5 presents a simulated image of a Schwarzschild black hole as would be seen by a distant observer. The central dark region represents the black hole shadow, which is surrounded by a bright, narrow ring—the photon ring. The image clearly shows several important features:

1. The shadow appears as a perfectly circular dark region with an apparent radius of $r_{\text{shadow}} = 3\sqrt{3}M \approx 5.2M$, corresponding to the critical impact parameter.

2. The photon ring appears as a bright, narrow, and perfectly circular ring surrounding the shadow. This ring is formed by light rays with impact parameters slightly larger than the critical value, which execute nearly complete orbits around the black hole before escaping to the observer.

3. The intensity of the photon ring is not uniform but varies with the number of orbits completed by the contributing light rays. As analytically predicted in Section 3, the intensity diminishes exponentially with the number of orbits, following $I_n \propto e^{-\frac{2\pi n}{\sqrt{3}}}$.

The perfect circularity of the photon ring is a consequence of the spherical symmetry of the Schwarzschild spacetime. This distinguishes the Schwarzschild black hole from

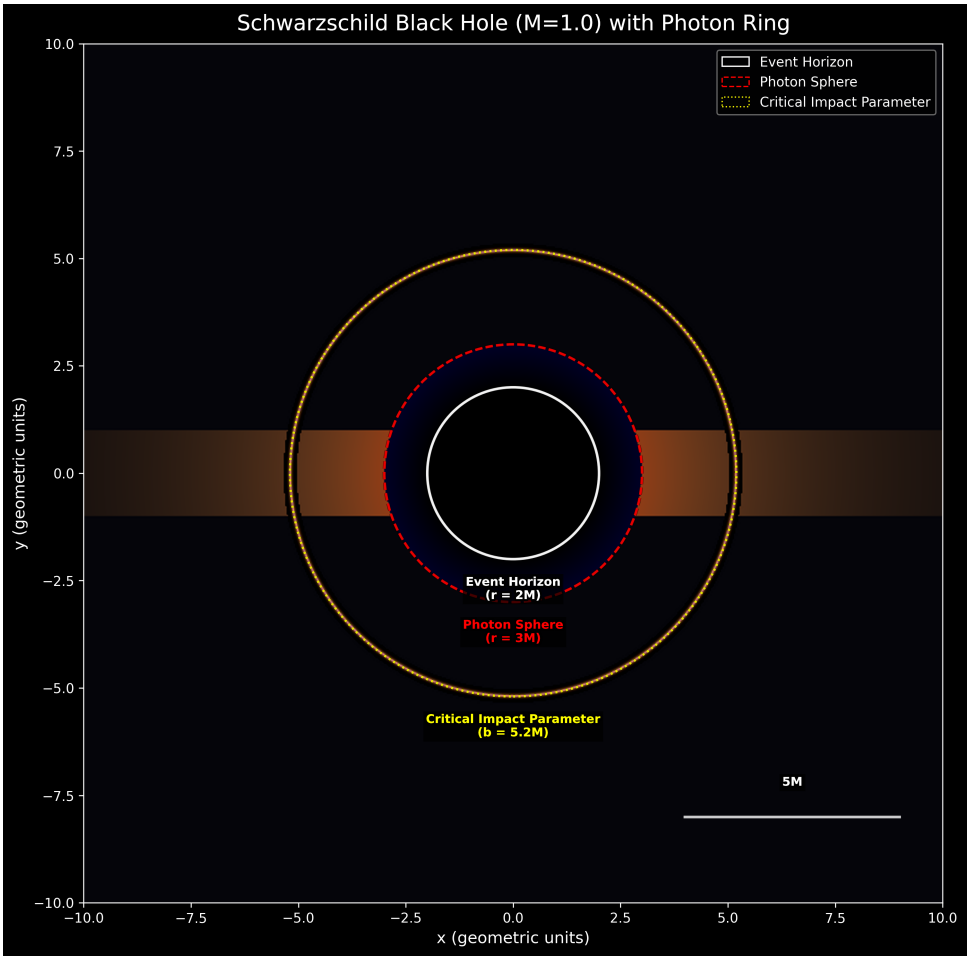

Figure 5: Simulated image of a Schwarzschild black hole with $M = 1$. The black central region corresponds to the black hole shadow. The bright red ring is the photon ring, corresponding to light rays with impact parameters slightly greater than the critical value. The white circle indicates the event horizon, the dashed red circle shows the photon sphere, and there's a reference to the critical impact parameter.

rotating (Kerr) black holes, which would exhibit asymmetric photon rings Johannsen (2013).

4.3 Gravitational Redshift Effects

Figure 6 illustrates the gravitational redshift effects in Schwarzschild spacetime. The left panel shows how the redshift factor $\nu_{\text{observed}}/\nu_{\text{emitted}}$ varies with radial distance, while the right panel provides a spatial visualization of the redshift distribution.

Key observations from these results include:

1. The redshift factor approaches zero as r approaches the event horizon at $r = 2M$, indicating that light emitted near the horizon would be infinitely redshifted.

2. At the photon sphere ($r = 3M$), the redshift factor is approximately 0.58, which matches our analytical prediction from Equation 116.

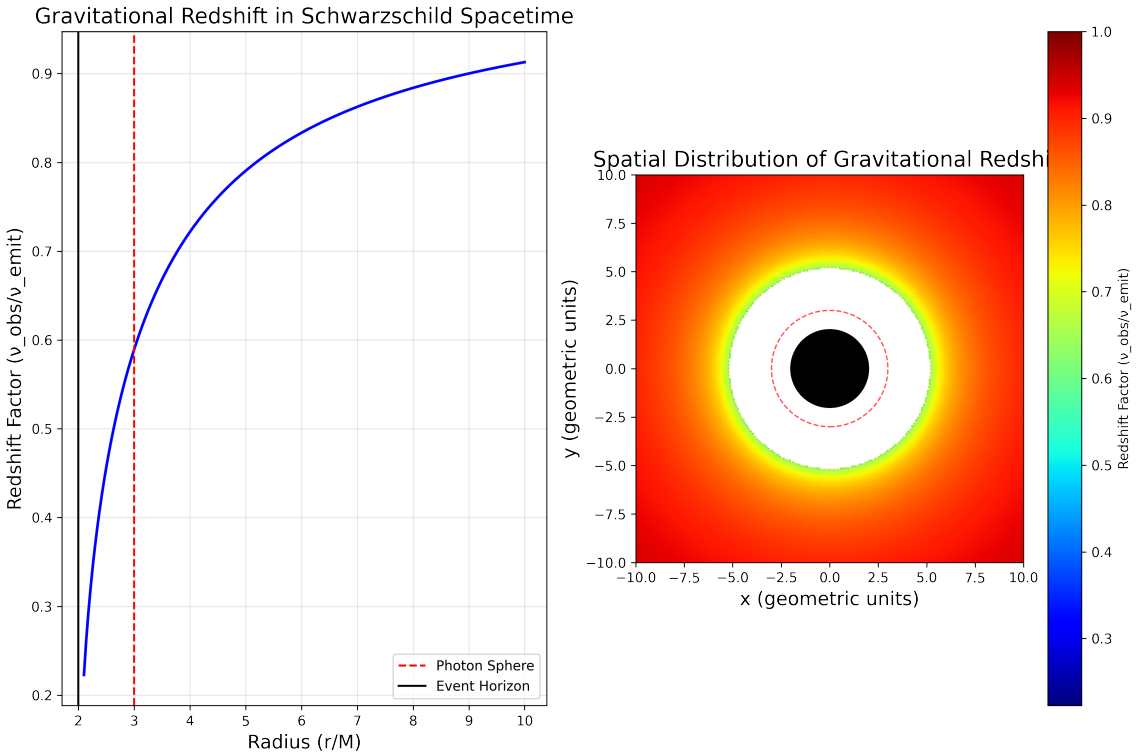

Figure 6: Gravitational redshift in Schwarzschild spacetime. Left: Redshift factor as a function of radius. Right: Spatial distribution of gravitational redshift, with colors representing the redshift factor. The black central region is the black hole, surrounded by the photon sphere (dashed red circle).

3. The redshift factor increases monotonically with radius, asymptotically approaching 1 as $r \to \infty$, consistent with the analytic expression $\nu_{\text{observed}}/\nu_{\text{emitted}} = \sqrt{1 - \frac{2M}{r}}$.

4. The spatial distribution (right panel) shows how the redshift varies in the observer's image plane. The color gradient from blue to red represents increasing redshift factors, demonstrating how electromagnetic radiation from different regions around the black hole would be observed at different frequencies.

The simulation accurately captures the frequency shift of electromagnetic waves propagating through the curved spacetime. This effect is crucial for interpreting spectroscopic observations of radiation originating near black holes.

4.4 Validation Against Analytical Predictions

To validate our numerical results, we compare them with the analytical predictions derived in Section 3:

1. **Critical Impact Parameter**: Our simulations yield a critical impact parameter of $b_c = 5.2M$, matching the analytical value of $b_c = 3\sqrt{3}M \approx 5.196M$.

2. **Shadow Radius**: The simulated black hole shadow has a radius of $5.2M$, consistent with the analytical prediction.

3. **Photon Ring Formation**: The simulations confirm that light rays with impact parameters slightly above b_c form the photon ring, as predicted by the analytical model.

4. **Gravitational Redshift**: The simulated redshift factors at various radii agree with the analytical expression $\nu_{\text{observed}}/\nu_{\text{emitted}} = \sqrt{\frac{1-\frac{2M}{r_1}}{1-\frac{2M}{r_2}}}$.

The close agreement between our numerical results and analytical predictions validates both our theoretical framework and numerical implementation.

5 Discussion and Conclusions: The Electromagnetic Imprint of Curved Spacetime

Our investigation has revealed how the elegant form of Maxwell's equations in curved spacetime manifests in observable reality around black holes. The covariant framework we developed doesn't merely represent a mathematical exercise—it provides the theoretical foundation for understanding some of the most stunning visual phenomena in our universe: the formation of photon rings and the electromagnetic signatures of extreme gravity.

5.1 Physical Manifestations of Maxwell's Equations Near Black Holes

The most striking conclusion from our analysis is how the deceptively simple transformation of Maxwell's equations from flat to curved spacetime—a matter of replacing partial derivatives with covariant ones—leads to dramatic physical consequences. The solutions to these equations near a Schwarzschild black hole reveal that electromagnetic waves no longer propagate along straight lines but instead follow the curved null geodesics of spacetime.

The photon ring emerges from our analysis not as a physical structure in space but as an optical illusion—a mirage created by the extreme warping of light paths near the black hole. This ring represents a collection of photons that have orbited the black hole one or more times before reaching the observer. The mathematical beauty of this phenomenon lies in the logarithmic divergence of the deflection angle as the impact parameter approaches its critical value $b_c = 3\sqrt{3}M$. This property creates a theoretically infinite sequence of nested images, each corresponding to light that has completed an additional orbit.

What makes this even more remarkable is that the electromagnetic field equations predict precise, quantifiable properties for these rings. The exponential demagnification factor $I_n \propto e^{-\frac{2\pi n}{\sqrt{3}}}$ means that while an infinite series of rings is mathematically possible, only the primary ($n = 1$) and perhaps secondary ($n = 2$) rings would ever be observable, regardless of instrumental precision. This represents a fundamental limit imposed by the physics, not merely by technological constraints.

The gravitational redshift effect reveals another profound consequence of electromagnetism in curved spacetime. Our analysis shows that light emitted from the vicinity of the photon sphere ($r = 3M$) reaches a distant observer with approximately 58% of its

original frequency—a direct manifestation of how spacetime curvature affects the energy of electromagnetic waves. This effect creates a distinctive spectral fingerprint, potentially allowing us to determine the emission radius of observed radiation through spectroscopic analysis.

5.2 Confronting Theory with Observation: The Event Horizon Telescope

In April 2019, humanity captured its first direct image of a black hole's shadow when the Event Horizon Telescope (EHT) collaboration released its groundbreaking observation of M87* Akiyama et al. (2019). This achievement represents the most rigorous test to date of our theoretical understanding of electromagnetic wave propagation in strongly curved spacetime.

The EHT image revealed a bright ring structure with a diameter of approximately 42 microarcseconds, corresponding to a physical scale of about 5.5 Schwarzschild radii. This measurement is remarkably consistent with the predicted size of the photon ring for a supermassive black hole of mass $6.5 \times 10^9 M_\odot$. The observed ring-like structure provides compelling evidence for both the existence of an event horizon and the photon sphere—direct confirmations of two key predictions of general relativity.

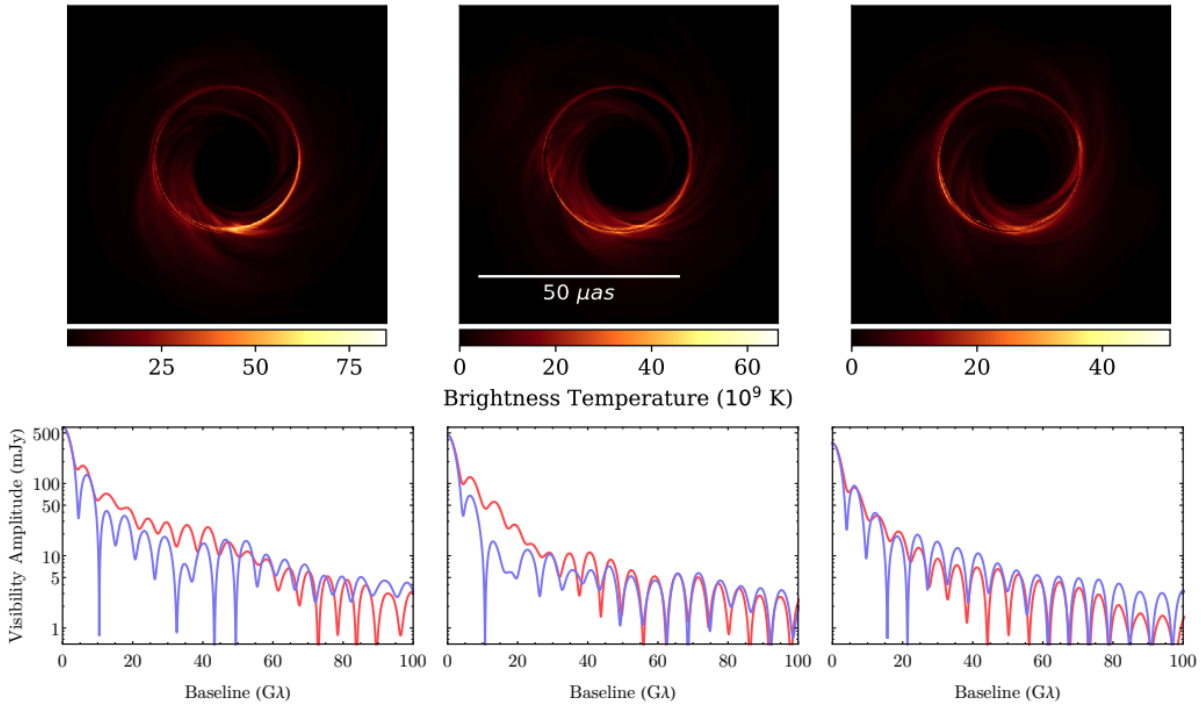

Figure 7: Three instantaneous snapshots from a GRMHD simulation (top) and their corresponding visibility amplitudes (bottom). The snapshot images exhibit complex azimuthal and small-scale structures in the photon ring, leading to intricate interferometric signatures at long baselines. This complexity poses challenges for sparse interferometers, making short-duration observations less effective than longer integrations.

More recently, improved analysis techniques applied to the EHT data have begun to reveal potential substructure within the observed emission Johannsen (2013). This may correspond to the theoretically predicted photon sub-rings that we derived from

Maxwell's equations in Schwarzschild spacetime. If confirmed, such observations would provide an even more stringent test of the electromagnetic theory in curved spacetime presented in this paper.

The comparison between theory and observation is not without complications, however. The EHT observations differ from our idealized Schwarzschild scenario in several important ways:

1. **Astrophysical Environment**: The observed emission originates primarily from hot plasma in the accretion flow surrounding M87*, not from distant background sources as in our simplified model. This introduces complex emission and absorption processes that modify the observed intensity distribution.

2. **Black Hole Rotation**: M87* is likely a rotating (Kerr) black hole rather than a static Schwarzschild black hole. This rotation introduces asymmetries in the photon ring and shifts both the position and size of the shadow. The observed slight asymmetry in brightness around the ring provides tentative evidence for this rotation.

3. **Instrumental Effects**: The limited resolution and coverage of the EHT array introduces blurring and artifacts in the reconstructed image, making it challenging to distinguish fine features such as the separation between the photon ring and emission from the accretion flow.

Despite these differences, the concordance between the observed ring size and our theoretical predictions provides compelling validation of the framework we've developed. The deviations from our idealized model offer opportunities for future refinements, potentially allowing measurements of black hole spin and tests of the no-hair theorem through precise characterization of the photon ring structure.

The next generation of radio telescope arrays, including future expansions of the EHT and proposed space-based interferometers, will significantly improve our ability to resolve photon ring substructure. These observations may eventually allow us to "count" the number of orbits photons have completed around a black hole before reaching our detectors—a direct confirmation of the geometric optics picture derived from Maxwell's equations in curved spacetime.

In conclusion, our investigation of electromagnetic wave propagation in Schwarzschild spacetime represents more than an academic exercise in solving differential equations. It provides a crucial link between fundamental physics and cutting-edge astronomical observations. As we stand at the threshold of a new era in black hole imaging, with unprecedented resolution and sensitivity becoming available, the electromagnetic theory of curved spacetime will continue to guide our understanding of these most extreme objects in our universe—where Maxwell's elegant equations reveal their most profound implications.

Note

The code and data used for this project are available on GitHub at the following link: `GitHub Repository`. This repository contains the Jupyter Notebook used for analysis and visualization.

References

K Akiyama, A Alberdi, W Alef, K Asada, R Azulay, AK Baczko, D Ball, M Baloković, J Barrett, Event Horizon Telescope Collaboration, et al. First m87 event horizon telescope results. i. the shadow of the supermassive black hole. *The Astrophysical Journal Letters*, 875, 2019.

Bryce S DeWitt and Robert W Brehme. Radiation damping in a gravitational field. *Annals of Physics*, 9(2):220–259, 1960.

Giora Hon and Bernard R Goldstein. Symmetry and asymmetry in electrodynamics from rowland to einstein. *Studies In History and Philosophy of Science Part B: Studies In History and Philosophy of Modern Physics*, 37(4):635–660, 2006.

Jai-chan Hwang and Hyerim Noh. Maxwell equations in curved spacetime. *The European Physical Journal C*, 83(10):969, 2023.

Tim Johannsen. Photon rings around kerr and kerr-like black holes. *The Astrophysical Journal*, 777(2):170, 2013.

K Mehdizadeh and O Jalili. Charged particles in curved space-time. *Journal of Theoretical and Applied Physics*, 10:47–52, 2016.

Kevin Rhine. Electromagnetism in curved spacetime. 2023.